

Controlled Synthesis of Heterogeneous Metal–Titania Nanostructures and Their Applications

Ran Liu and Ayusman Sen*

Department of Chemistry, The Pennsylvania State University, University Park, Pennsylvania 16802, United States

S Supporting Information

ABSTRACT: We describe a new synthetic approach to heterogeneous metal–TiO₂ nanomaterials based on conversion of Ti³⁺ to hydrous TiO₂ occurring uniquely on the nanostructured metallic surfaces such as Pt, Au, and Ni nanowires and nanoparticles. The TiO₂ growth mechanism was studied by designing an electrochemical cell. A variety of heterogeneous metal–TiO₂ nanostructures, such as segmented metal–TiO₂ nanowires, core–shell metal–TiO₂ nano/microparticles, and composite metal–TiO₂ nanotubes, can be fabricated by varying the morphology of the seeding metal nanostructure or controlling selective TiO₂ growth on different surfaces of the metallic nanomaterial. Altering the reaction time and Ti³⁺ concentration allows the TiO₂ segment lengths or TiO₂ shell thicknesses to be finely tuned. Coaxial Au–TiO₂ nanorod arrays were demonstrated to be fast lithium-ion storage materials, while the core–shell Ni–TiO₂ nanoparticles exhibited excellent photodegradation properties as magnetic recyclable photocatalysts.



INTRODUCTION

Nanostructured titanium dioxide (TiO₂) is of great current interest owing to the excellent optical and photocatalytic properties of TiO₂ itself as well as the added benefits derived from the smaller sizes of nanomaterials.¹ Application of the material in dye-sensitized solar cells,^{2–4} water splitting,^{5–7} photodegradation of organics,^{8–10} and electrochromic devices^{11,12} has been reported extensively. To date, synthesis of TiO₂ nanomaterials has relied on sol–gel,^{13–15} surfactant-directing,^{16–18} hydrothermal,^{19–21} electrochemical deposition,^{22–25} Ti film anodization,^{26–28} and atomic layer deposition (ALD)²⁹/chemical vapor deposition (CVD)³⁰ methods. In this paper, we report a new synthetic approach based on oxidative conversion of Ti³⁺ to hydrous TiO₂ occurring uniquely on nanostructured metallic surfaces such as Pt, Au, and Ni nanowires and nanoparticles. This method allows us to fabricate various TiO₂–metal heterogeneous nanostructures, which can exhibit synergistic properties and multifunctionalities arising from each of its nanocomponent^{31,32} For example, previous studies showed that the enhanced photodegradation efficiency,^{9,33,34} water-splitting efficiency,⁵ and hydrazine sensitivity³⁵ can be achieved by Pt–TiO₂ cocatalysts⁹ such as Pt–TiO₂ nanowires/nanofibers^{33,35} and core–shell nanoparticles.³⁴ Gold clusters on TiO₂ have been studied for catalytic CO oxidation.³⁶ Mesoporous Au/TiO₂ has shown enhanced photocatalytic properties.³⁷ Nickel-modified TiO₂ nanotubes^{38,39} have been employed as electrodes for methanol oxidation.³⁹ Ag–TiO₂ core–shell nanoparticles⁴⁰ or Ag-loaded TiO₂ nanotubes⁴¹ were also studied for their photocatalytic properties. Here, we report the application of core–shell TiO₂–Ni nanoparticles as a magnetic recoverable photocatalyst for degradation of methylene blue (MB) and use of coaxial

Au–TiO₂ nanorod array as a fast electrochemical energy storage material.

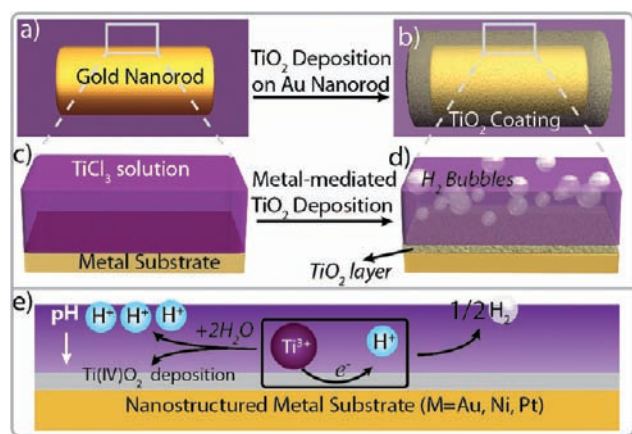
The synthetic method described in this paper offers several advantages: First, it is a versatile method for the synthesis of different types of heterogeneous nanostructures. For example, TiO₂ can be selectively deposited on the ends of metal nanowires to form segmented TiO₂–metal nanowires or to fully cover metal nanorods to form core–shell nanoparticles or be deposited around metal nanoparticles on the wall of nanosized channels to form composite TiO₂–metal nanotubes. Second, by varying the reaction time and TiCl₃ concentration, the TiO₂ segment length and TiO₂ shell thickness can be finely controlled. Finally, the reaction is simple and requires no surfactant, no heating, and no electricity. It can be applied to any nanostructured Pt, Au, and Ni (or other metals that are in electrical contact with one of these three) surface. Since the deposition occurs only on the nanostructured metal seed, random TiO₂ nucleation and growth in solution can be avoided, a problem possibly associated with hydrolyzed^{40,42,43} or sol–gel TiO₂ coating on metal nanoparticles or polystyrene spheres.⁴⁴

RESULTS AND DISCUSSION

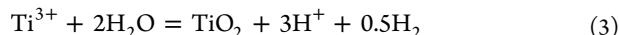
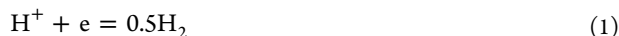
Scheme 1 illustrates the TiO₂ growth mechanism occurring on nanostructured metal surfaces. First, the pH of TiCl₃ solution needs to be adjusted to around 2.5 under anaerobic conditions. Lower pH increases the solubility of TiO₂, thereby preventing its deposition. On the other hand, too high a pH will result in uncontrolled deposition of TiO₂ from solution. When selected

Received: January 5, 2012

Published: April 23, 2012

Scheme 1. TiO₂ Growth Mechanism on Nanostructured Metal Surfaces

nanostructured metal surfaces are exposed to TiCl₃ solution, hydrogen bubbles are formed and hydrous TiO₂ is deposited on the metal surface (Scheme 1d). The deposited TiO₂ can be further annealed at 400–500 °C to form anatase. The half reactions involved in formation of TiO₂ are shown in eqs 1 and 2, leading to the overall reaction shown in eq 3. The required electron transfer between Ti³⁺ and H⁺ is presumably mediated by specific nanostructured metal surfaces (see below).



We tested five different nanostructured metals: Pt, Au, Ag, Cu, and Ni. Of these, only Pt, Au, and Ni are active for catalyzing TiO₂ growth (see Supporting Information, Figure S1 for the silver nanowires before and after exposure to TiCl₃). This is due to the known lower overpotential for H⁺ reduction to hydrogen (eq 1) on the surfaces of nanostructured noble metals such as Pt and Au as well as electrodeposited Ni.⁴⁵ No TiO₂ deposition was observed on bulk Pt, Au, and Ni films. Figure 1 compares the reactions of 50 mM TiCl₃ solution with alumina templates that have been sputtered with Pt and Cu.

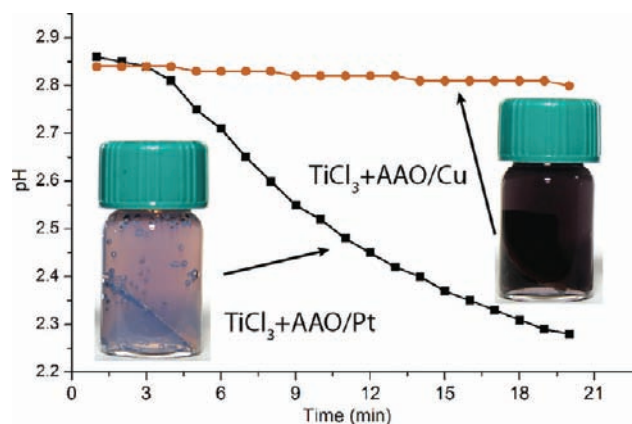


Figure 1. pH profiles over time for the alumina template sputtered with Pt and Cu and contacted with 50 mM TiCl₃ solution: AAO/Pt (left bottle) and AAO/Cu (right bottle). Bottles were sealed under nitrogen.

During sputtering, metal nanoparticles form inside the walls of nanosized channels in the template. As shown, when Pt-loaded alumina template is exposed to 50 mM TiCl₃ for 5–10 min bubbles are formed on the wall of the glass bottle. At the same time, the color of the solution becomes lighter as the Ti³⁺ is consumed and the pH of the solution drops (see eq 3). The corresponding Cu-loaded alumina template exhibits no gas formation, no color change, and no drop in pH.

Figure 2 shows various structures obtained by TiO₂ growth on the ends of anodized aluminum oxide (AAO)-shielded metallic nanowires. By controlling the growth on one end of the metal nanowire, segmented metal–TiO₂ nanowires can be obtained. For example, the TEM image and energy-dispersive X-ray spectroscopy (EDS) line scan profile for a Ni–TiO₂ nanowire are shown in Figure 2c. The Pt–TiO₂ nanowires SEM image is presented in Figure 2d. All images were taken after annealing to convert the TiO₂ segments to anatase. Loss of water during annealing results in shrinkage of the TiO₂ segment and a smaller diameter than the metal nanowires from which it grew. Such bisegmented Pt–TiO₂ nanowires may find application as light-driven nanomotors.⁴⁶ The TEM image of the TiO₂ segment can be seen in Figure 2e. The high-resolution TEM image of TiO₂ is shown in Figure 2g; the lattice spacing matches very well with the (101) peak of the anatase X-ray diffraction (XRD) profile. By exposing both ends of the metal nanowire to the TiCl₃ solution, TiO₂–Metal–TiO₂ can be fabricated. Such nanostructures where both ends of the metal nanowire are protected are of current interest for nanowire self-assembly.^{47,48} Figure 2h shows a Pt nanowire capped with thin layers of TiO₂ on both ends. Figure 2f shows the top view of concentric circles from TiO₂-capped Pt nanowires. Figure 2i shows the pure TiO₂ nanowire after the gold nanowire template is etched away by iodine/iodide solution.

Figure 3 shows the remarkably linear relationship between the growth of TiO₂ nanowire on the end of a Au nanowire and reaction time at a fixed TiCl₃ concentration of 0.7 M. From the plot a uniform growth rate of 1.9 μm/h can be calculated. Thus, the rate of TiO₂ growth does not decrease even when the metal surface is already covered by TiO₂. This suggests that the deposited hydrous TiO₂ is both electrically conductive and permeable to protons (see Figure 3d). In addition, the TiO₂ formed on the metal surfaces is highly porous, allowing the hydrogen gas to diffuse out. The specific surface area and pore-size distribution of the synthesized TiO₂ were measured and are discussed below.

To further probe the TiO₂ formation mechanism we designed an electrochemical cell that separates the two half reactions shown in eqs 1 and 2. Figure 4a shows the setup of such a short-circuited electrochemical cell involving pre-electrodeposited nanowire-loaded alumina template as the cathode and indium tin oxide (ITO) glass as the anode. The short-circuited currents were measured by a potentiostat. The current density is limited by the AAO/metal nanowire electrode, which has a smaller area than the ITO glass. Results show that for predeposited Pt, Au, and Ni, the steady current was much higher than that for Ag and Cu. Consistent with this observation, the ITO glass was only coated with transparent TiO₂ film when the first three metals served as the cathode.

By calculating the charge passed between the two electrodes in the above setup we can estimate the amount of TiO₂ deposited based on the Faradaic law

$$m(\text{TiO}_2) = QM/F \quad (5)$$

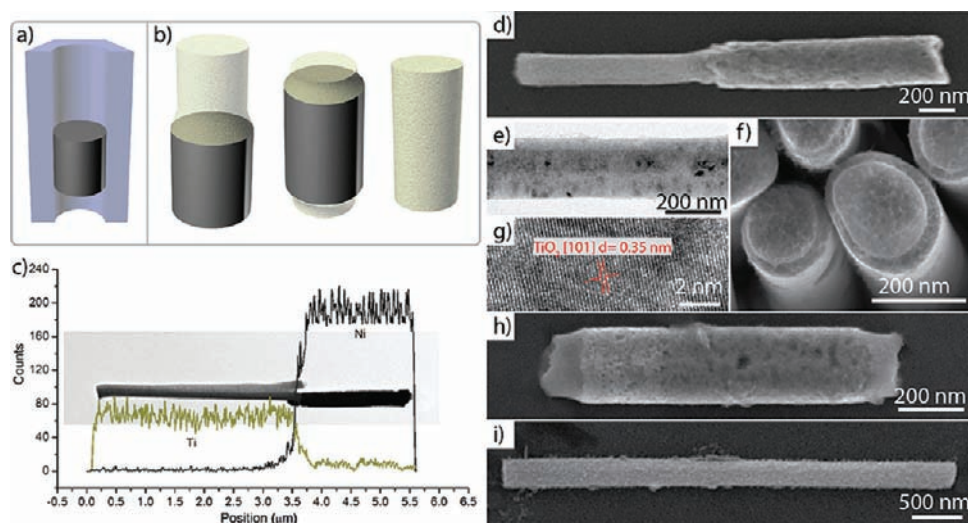


Figure 2. TiO₂ growth on nanostructured metal structures whose sides are shielded by AAO: (a) metallic seed in AAO, (b) different TiO₂–metal nanostructures, (c) TEM image and EDS profiles of segmented TiO₂/Ni nanowire, (d) SEM image of segmented TiO₂/Pt nanowire, (e) TEM image of TiO₂ segment, (f) SEM top view of short TiO₂ cap growth on metallic nanowire (exposed to 50 mM TiCl₃ solution for 10 min), (g) high-resolution TEM image of TiO₂ segment, (h) SEM of Pt nanowire with both end capped by TiO₂, and (i) pure TiO₂ nanowire.

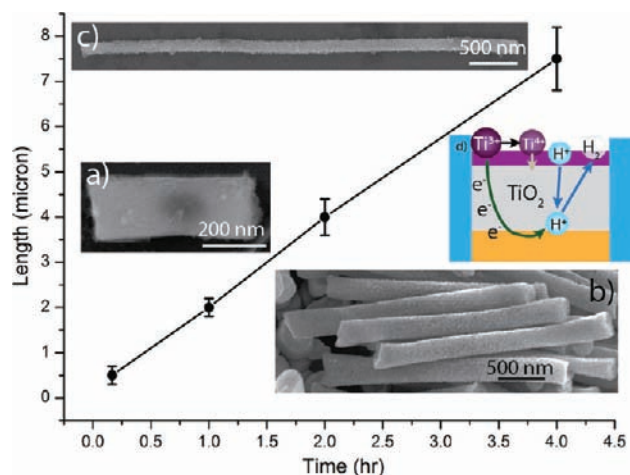


Figure 3. Growth of TiO₂ nanowire on the end of a Au nanowire versus reaction time (TiCl₃, 0.7 M): (a) 10 min, (b) 1 h, (c) 4 h, and (d) continued TiO₂ growth mechanism on Au nanowires.

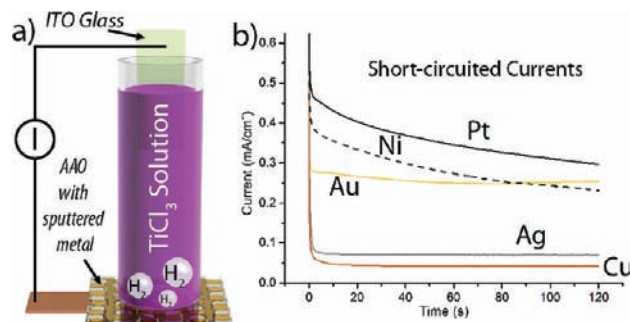


Figure 4. (a) Illustration of the electrochemical cell for measuring short-circuited currents between the metal nanowire-loaded alumina template and ITO glass in 0.7 M TiCl₃. (b) Short-circuited current profiles over the time for different metal nanowires.

where $m(\text{TiO}_2)$ is the mass of TiO₂, Q is the charge, M is the molecular weight of TiO₂, and F is the Faraday constant. The same relationship holds for TiO₂ deposited on AAO/metal

nanowires in the absence of ITO because of identical redox chemistry.

Thus, based on the density of TiO₂ and the electrode area we can estimate the thickness of the deposited TiO₂ on ITO and by extension the lengths of the TiO₂ segments on the metal ends in AAO

$$L(\text{TiO}_2) = QM/(Fsd) \quad (6)$$

where $L(\text{TiO}_2)$ is the nanowire length, Q is the charge, M is the molecular weight of TiO₂, F is the Faraday constant, S is the electrode area (the exposure area of AAO pores, 0.2 cm²), and d is the density of TiO₂.

For example, using the current profile for Au/AAO the charge passed after 2 min is approximately 6.5 mC and the thickness of TiO₂ on 0.2 cm² electrode should be around 65 nm. Therefore, the growth speed can be estimated to be 2 μm/h, a number that is remarkably close to that obtained from Figure 3 for deposition on Au nanowires.

By coating TiO₂ on the metal nanoparticles after template removal core–shell metal–TiO₂ nanoparticles can be obtained, as shown in Figure 5a. By selective etching the core material (e.g., Au core can be etched by I₃[−]), hollow TiO₂ nanocapsules can be fabricated. Figure 5b showed the SEM image of an Au nanorod coated with TiO₂ on the surface. The internal structures are revealed by the TEM in Figure 6d. The TiO₂ shell mirrors the shape of the interior Au nanorod. The EDS line profile further establishes the core–shell nanostructure (Figure 5d). Figure 5c shows the TEM image of a TiO₂ nanocapsule after the Au core was removed. No residual Au was found by EDS analysis (data not shown).

By controlling the TiO₂ coating time or TiCl₃ concentration the thickness of the TiO₂ shell can be tuned (Figure 6). Thin TiO₂ shell more resembles the original shape of the inside nanowire; sharp edges of TiO₂ shell can be seen on the end of the nanoparticle (Figure 6a). As the TiO₂ shell thickness increases the end of the core–shell nanoparticle becomes more rounded (Figure 6b) and finally evolves into an egg-shaped micrometer-sized particle (Figure 6c and 6d). The shell thickness also affects the properties of core–shell metal–

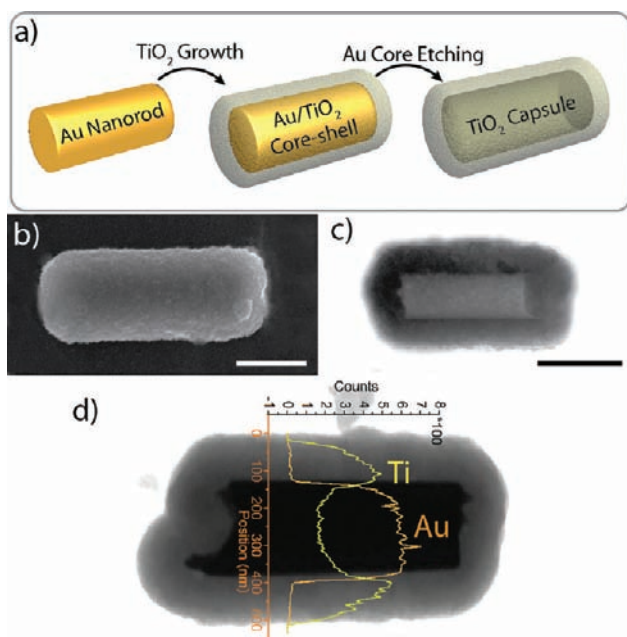


Figure 5. Core-shell Au-TiO₂ nanoparticle synthesis: (a) synthetic scheme, (b) SEM image, and (c) TEM image of hollow TiO₂ nanocapsule after Au core is removed. (d) TEM image and EDS line profile for 2b (scale bar 500 nm) (the core-shell nanoparticles were obtained by exposing Au nanorods in 0.2 M TiCl₃ solution for 10 min).

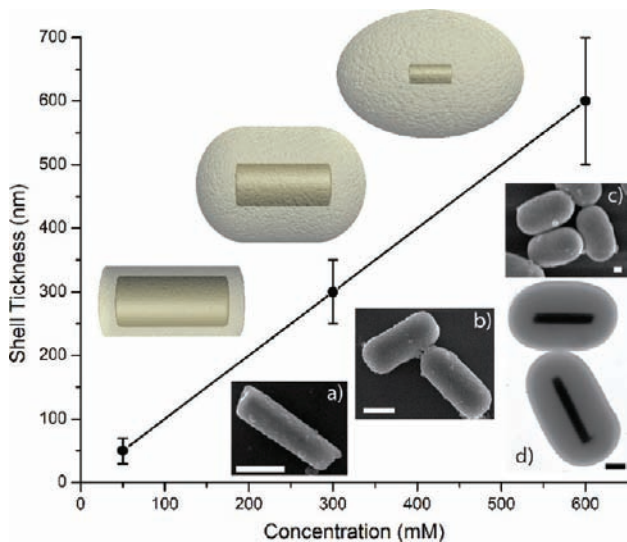


Figure 6. Shape evolution of TiO₂-Pt core-shell nanoparticles versus TiCl₃ concentration. SEM (a-c) and TEM (d) images of Au nanorods after exposed in (a) 50 mM TiCl₃, (b) 300 mM TiCl₃, and (c and d) 700 mM TiCl₃ for 10 min (scale bar 500 nm).

TiO₂ nanoparticles, such as photodegradation rate and lithium-ion insertion efficiency (see below).

Metal nanoparticles loaded onto the wall of the alumina template can also be used as seeds to grow composite TiO₂-metal nanotubes (Figure 7a and 7b). For example, when the alumina template is sputtered with metal by plasma the metal enters the pores of alumina template and deposits on the walls of alumina template. By exposing these nanotubes in 50 mM TiCl₃ solution for 5–10 min, thin composite TiO₂-metal nanotube can be obtained. (a higher concentration of TiCl₃

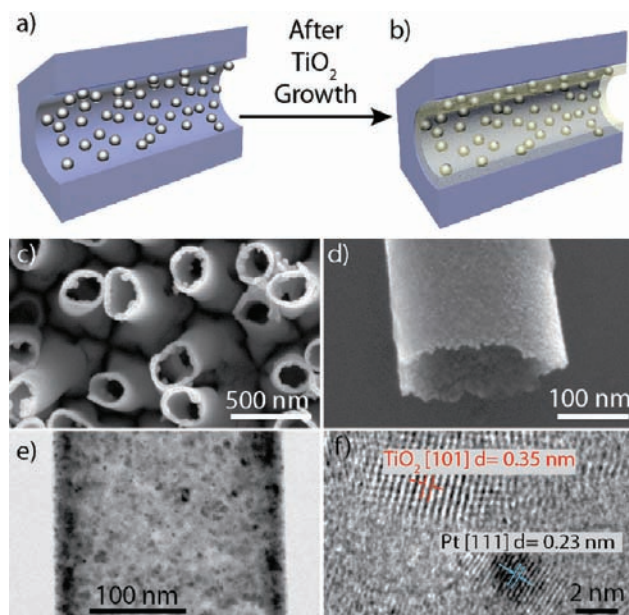


Figure 7. Composite TiO₂-Pt nanotubes synthesis: (a and b) synthetic scheme, (c) top view of composite nanotubes array by SEM, (d) SEM image of the opening end of TiO₂-Pt composite nanotube, (e) TEM image of the side view, and (f) high-resolution TEM.

leads to formation of solid nanowires, as TiO₂ growth is very fast due to the high surface area of sputtered metallic nanoparticles). After annealing the composite nanotubes at 400–500 °C, the alumina template can be removed to expose these nanotubes. Figure 7c shows the openings of free-standing TiO₂-Pt nanotube array. As can be seen the wall thickness of these nanotubes is quite uniform. High-resolution SEM reveals that the surface morphology of the nanotube is very rough with numerous of nanoparticles (Figure 7d). TEM images show that the Pt nanoparticles are evenly distributed over the entire composite nanotube (Figure 7e and Supporting Information, Figure S2 for the dark-field TEM image). High-resolution TEM shows a lattice spacing of a darker smaller particle that matches well with the (111) peak of the Pt XRD pattern, while a larger lattice spacing matches the (101) peak of the anatase XRD pattern. These composite nanotubes are expected to show enhanced photocatalytic properties as the Pt nanoparticles embedded in TiO₂ nanotube induce formation of a Schottky barrier, leading to fast transport of photogenerated electrons to the Pt nanoparticles (better charge separation).³³

Although the silver and copper nanomaterials are not active in catalyzing TiO₂ growth, they can be combined with Pt, Au, or Ni as seeds to initiate TiO₂ deposition. Figure 8a and 8b shows the TiO₂ growth scheme on a Pt-Ag segmented nanowire. On the basis of the activity test (Figure 4b) one would expect the TiO₂ to selectively deposit on the Pt segment alone (See Supporting Information, Figure S1.). However, as shown, both Ag and Pt surfaces are covered uniformly by TiO₂. This suggests that while only Pt catalyzes reduction of H⁺ to hydrogen, deposition of TiO₂ can occur on both metals because they are in electrical contact and the electron flows freely from Pt to Ag. Figure 8c shows the TEM image of a Pt-Ag/TiO₂ core-shell particle. On the basis of the EDS line profiles, only a very small tip of Pt (length ratio of Pt to Ag is around 1:10) can lead to formation of a uniformly thick TiO₂ shell on both metals.

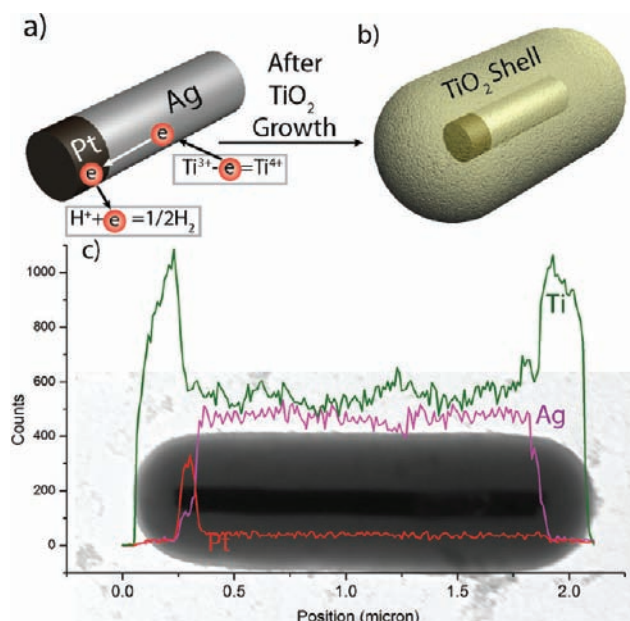


Figure 8. (a and b) Synthesis of core-shell (Pt–Ag)/ TiO_2 nanoparticle by TiO_2 growth on a Ag–Pt segmented nanowire. (c) TEM image and EDS elemental line profiles (Ti, Ag, and Pt).

Recently, TiO_2 and TiO_2 -based materials have been demonstrated as promising anode materials in rechargeable lithium-ion batteries.^{49–52} TiO_2 has the virtues of being chemically stable, inexpensive, nontoxic, and environmentally benign. The charge/discharge (i.e., Li-ion insertion/extraction) process of TiO_2 can be expressed as follows, where x is the Li-ion insertion coefficient



Figure 9 demonstrates application of a coaxial Au– TiO_2 nanorods array in fast lithium-ion battery electrode materials. These coaxial Au– TiO_2 nanorods were synthesized by

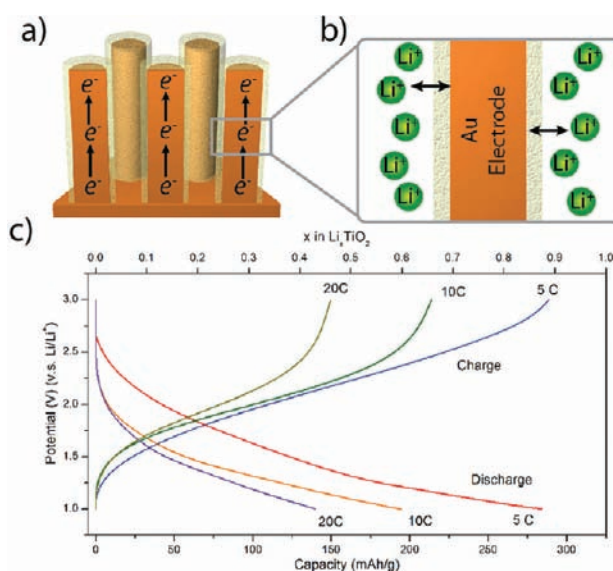


Figure 9. (a and b) Lithium-ion storage mechanism for the TiO_2 -coated Au nanorods array. (c) Galvanostatic charge/discharge curves at different charge/discharge rates (Au nanorods were electro-deposited at -0.9 V after 1 C charge has passed per cm^2).

immersing the Au nanorods in 25 mM TiCl_3 for 10 min. No annealing was performed after TiO_2 growth. The formed amorphous TiO_2 shells allow faster Li-ion transport.⁴⁹ Figure 9a and 9b shows the lithium-ion storage mechanism. The Au nanorods are highly conductive, which facilitate electron transfer between the electrode bottom and the TiO_2 shells (Figure 9a). In addition, they provide mechanical support to the thin TiO_2 shells. The thin TiO_2 shells allow fast lithium-ion insertion–desorption owing to the short Li-ion pathways (Figure 9b). As shown in Figure 9c, the charge/discharge capacity (which can be estimated/calculated based on the charge/discharge curve and the weight of the TiO_2 electrode, see Supporting Information, Figure S3 and note) of the TiO_2 is well maintained even at a high charge/discharge rate. At 5 C the charge capacity of the shell TiO_2 is 280 mAh/g (corresponding to a Li-ion insertion coefficient of 0.84), which is higher than that found for heterogeneous TiO_2 nanostructures (TiO_2 –carbon nanotube,⁵⁰ TiO_2 –graphene,⁵¹ TiO_2 – RuO_2 nanocomposite⁵²) at similar charge/discharge rates. On the basis of the charge/discharge capacities at different charge/discharge rates we calculated the energy densities at different power densities, and the results are shown as a Ragone plot (see Supporting Information, Figure S4), which reveals that the energy density is well maintained even at a high power density of 1.3 kW/kg (corresponding to a charge/discharge rate of 5C). Cyclic voltammetry was also used to study Li-ion insertion into the TiO_2 shell, and the result is shown in Supporting Information, Figure S5. We investigated the effect of TiO_2 shell thickness on the charge capacity (see Supporting Information, Figure S6). A shorter TiO_2 coating time (5 min) leads to formation of a very thin TiO_2 shell (10 nm), which exhibits an even higher charge capacity (ca. 300 mAh/g). A longer reaction time (20 min) leads to TiO_2 completely filling up the narrow space (less than 100 nm) between the Au nanorods. This drastically reduces the accessibility of the electrolyte to the electrode material. The lithium-ion diffusion path becomes significantly longer (see Supporting Information, Figure S6b). As a result, the charge/discharge capacity decreases to 150 mAh/g at a high charge/discharge rate of 5C. We also performed the cycling test on the TiO_2 -coated Au nanorods (see Supporting Information Figure S7). The result shows that 90% of the charge/discharge capacity is maintained after 100 cycles.

Figure 10 shows the photodegradation of methylene blue (MB) using Ni– TiO_2 core-shell nanoparticles (Ni– TiO_2 CSN) as recyclable⁵³ photocatalysts. The Ni– TiO_2 CSN were synthesized by exposing the Ni nanowires (2 μm) in 0.7 M TiCl_3 for 10 min (only 100 nm thick TiO_2 shell is formed because of the slow TiO_2 growth rate). No subsequent annealing was performed. The multicomponent Ni– TiO_2 CSN exhibit multifunctionalities arising from the synergic properties of each component (Figure 10a): The amorphous TiO_2 shell can photodegrade MB under UV irradiation while preventing the Ni core from corrosion. The Ni core allows recycling of Ni– TiO_2 CSN since it can be easily separated by applying a magnetic field. Similar magnetic responsive Fe_3O_4 – TiO_2 hollow capsules have been previously reported.⁵⁴ Figure 10b and 10c shows the MB aqueous solution dispersed with Ni– TiO_2 CSN before and after UV irradiation in a quartz cuvette. After 40–50 min of UV irradiation the color of the MB solution disappeared. Supporting Information Figure S8 shows the decrease in UV–vis absorption of a methylene blue solution after being exposed to UV photoirradiation for varying periods

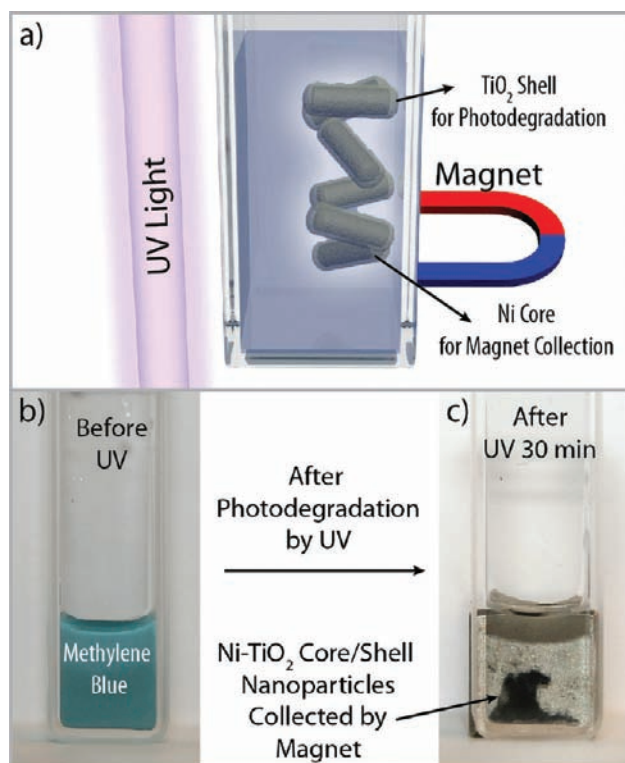


Figure 10. Photodegradation of methylene blue (MB) by Ni-TiO₂ CSN under UV irradiation: (a) scheme for multifunctional Ni-TiO₂ CSN, (b) MB aqueous solution dispersed with Ni-TiO₂ CSN before UV irradiation, and (c) photodegraded MB solution by Ni-TiO₂ CSN after 45 min UV irradiation and Ni-TiO₂ CSN were collected by a magnet.

of time in the presence of core-shell Ni-TiO₂ nanoparticles. The Ni-TiO₂ CSN were then collected by the magnet behind the quartz cuvette. We compared the performance of Ni-TiO₂ CSN and the commercial TiO₂ nanoparticles (25 nm) for the photocatalytic degradation. The result shows that at the same amount of catalyst loading the amorphous TiO₂ shells show a significantly higher photodegradation rate than the commercial crystalline TiO₂ nanoparticles (see Supporting Information, Figure S9). The high photodegradation rate is due to the high surface area of the TiO₂ shell. BET measurements reveal that the surface area of the TiO₂ CSN is 120.7 m²/g with a typical pore size of ca. 11.3 nm, while the commercial TiO₂ nanoparticle has a surface area of 39.2 m²/g with a typical pore size of ca. 22.1 nm. The pore-size distribution of these two materials can be found in Supporting Information, Figure S10. In order to study the effect of TiO₂ shell thickness on the photodegradation properties, we coated the Ni nanowires with TiO₂ for 20 min in 0.7 M TiCl₃. As expected, a thicker TiO₂ shell (200 nm) is obtained. Due to its high porosity, even the thicker TiO₂ shell maintains the high surface area while allowing more photocatalyst to be loaded. As a result, the photodegradation rate is approximately doubled (Supporting Information, Figure S9).

CONCLUSION

We discovered a new synthetic approach to heterogeneous metal-TiO₂ nanomaterials via Ti³⁺ oxidation occurring uniquely on nanostructured metal surfaces. Electron transfer between Ti³⁺ and the protons is mediated and catalyzed by the

metal surface due to a low overpotential for proton reduction to hydrogen gas. Five different metal nanomaterials (Au, Pt, Ni, Ag, and Cu) were tested: only Au, Pt, and Ni are active for TiO₂ deposition. By varying the morphology of the seeding metal nanostructures as well as by controlling selective TiO₂ growth on different surfaces of metal nanomaterials, segmented metal-TiO₂ nanowires, core-shell metal-TiO₂ nano/microparticles, and composite metal-TiO₂ nanotubes can be fabricated. TiO₂ segment length or TiO₂ shell thickness can be tuned by varying Ti³⁺ concentration and reaction time. Coaxial Au-TiO₂ nanorod arrays were demonstrated to be fast lithium-ion storage materials, while the core-shell Ni-TiO₂ nanoparticles can be utilized as magnetic recyclable photocatalysts. The synthetic approach described lends itself to design and fabrication of other novel metal-TiO₂ heterogeneous nanostructures. For example, by tuning the shapes of the metal seeds, other metal-TiO₂ nanostructures can be fabricated. Mesoporous TiO₂ can be deposited from the TiCl₃ solution with a proper amount of surfactant added. In addition, functional nanomaterials such as quantum dots can also be incorporated into the TiO₂ matrix during deposition. Such heterogeneous nanostructures may exhibit synergistic multifunctional properties.

EXPERIMENTAL DETAILS

Chemicals and Materials. Copper sulfate pentahydrate (CuSO₄·5H₂O), ammonium sulfate [(NH₄)₂SO₄], diethylenetriamine (DETA), silver chloride (AgCl), sodium thiosulfate (Na₂S₂O₃), potassium pyrosulfite (K₂S₂O₅), sodium hydroxide (NaOH), sodium carbonate (Na₂CO₃), ethylene carbonate (EC), diethyl carbonate (DEC), lithium hexafluorophosphate (LiPF₆), nitric acid (HNO₃), methylene blue (MB), and TiO₂ nanoparticles (25 nm) were purchased from Sigma Aldrich. Titanium(III) chloride (20% in 3% HCl) was obtained from Alfa Aesar. Platinum TP plating solution, gold Ortemp 24 plating solution, and nickel sulfamate plating solution were commercially available from Technic, Inc. Silver plating solution was made by mixing silver chloride (50 g/L), sodium thiosulfate (500 g/L), and potassium pyrosulfite (30 g/L). Copper plating solution was made by mixing copper sulfate pentahydrate (100 g/L), ammonium sulfate (20 g/L), and diethylenetriamine (80 mL/L). Copper etchant (BTP) was obtained from Transene. Indium tin oxide (ITO)-coated glass (sheet resistance 5–10 Ohms) was purchased from Delta Technologies. Anodized aluminum oxide (AAO) membrane with 200 nm pore size was commercially available from Whatman. Carbon film-supported gold/nickel/copper TEM grids (200 mesh) were purchased from Electron Microscope Sciences. Deionized water was made by a Barnstead Nanopure Diamond Water system. All chemicals were used as received, and solutions were freshly prepared.

Synthesis. Platinum (or Gold) Nanorods. AAO membrane was sputtered with silver (200 nm) using a Kurt Lesker CM-18/RF sputtering system. Then silver was first electrodeposited from silver plating solution into the alumina membrane (to seal the pores) by applying a -0.5 mA/cm² current density for 10 min on the potentiostat SP-150 from Biologic. After silver deposition the Pt was subsequently electrodeposited from the commercial Technic Platinum TP solution at a current density of -1 mA/cm². A 50 min deposition grows around 1 μm platinum segment. Ag/AgCl served as the reference electrode, and platinum foil was used as a counter electrode, if not specified otherwise. After growth of platinum in the alumina membrane, HNO₃ (4 M) was applied to etch off the sputtered/electrodeposited silver. Pt nanorods were released by dissolving alumina membrane in 3 M sodium hydroxide. The obtained Pt nanorods were centrifuged and washed repeatedly at least 8 times and finally dispersed in deionized water at a desired concentration. Au nanorod synthesis follows the same procedure except Au was electrodeposited (-0.9 V from gold plating solution) after Ag.

Silver (or Nickel) Nanowires. Alumina template was sputtered with copper (200 nm). Then copper was first electrodeposited into the alumina membrane by applying -1.2 V for 2 min from copper plating solution to seal the pores. After copper deposition Ag was subsequently electrodeposited from silver plating solution at a current density of -1 mA/cm² for 30 min. Copper etchant BTP was applied to etch off the sputtered/electrodeposited copper. Ag nanowires were released by dissolving alumina membrane in 3 M sodium hydroxide. Nickel nanorods synthesis follows the same procedure except the Ni was electrodeposited (-1 mA/cm² from nickel plating solution) after copper.

TiO₂ Deposition. First, under nitrogen protection, saturated Na₂CO₃ solution was added to the original TiCl₃ solution drop by drop while stirring until the pH was around 2.5 and the resulting TiCl₃ concentration was around 0.7 M. Such solution can be used directly or diluted by 3 mM HCl to desired concentration. For synthesis of metal–TiO₂ segmented nanowires or metal–TiO₂ composite nanotubes, metal-loaded alumina membrane (by sputtering or electrodeposition) was simply soaked or selectively exposed to the TiCl₃ solution under a nitrogen-protected environment. After TiO₂ was deposited for a certain period of time, annealing (450 °C) can be done using a tube furnace (Lindberg/Blue Mini-Mite) under nitrogen protection for 4 h. Then the alumina membrane is etched away by 3 M NaOH to release nanomaterials. For the core–shell metal–TiO₂ nano/microparticles synthesis, metal nanoparticles seeds were first extracted from water by centrifuge. Then the upper level water was pipetted out, and neutralized TiCl₃ was immediately added. Brief sonication was applied to disperse the metal nanoparticle seeds. Stirring was applied while the TiO₂ was depositing on the seeds under nitrogen protection. After a desired growth time, the solution was filtered by Costar Spin-X Centrifuge Tube Filter (0.22 μm nylon) under vacuum suction. The final obtained core–shell metal–TiO₂ particles was rinsed and dispersed in DI water. For the Au–TiO₂ core–shell nanorods array electrodes, after the Au nanorods were electrodeposited in the alumina template, the template was removed by 3 M NaOH to expose the Au nanorods. Then the TiCl₃ solution (25 mM) was applied to the Au nanorods for 10 min to coat them with TiO₂. The electrode was then dried in an oven overnight at 150 °C to completely remove the surface water.

Characterization. pH Measurement. Copper- or platinum-sputtered alumina template was soaked in the 50 mM TiCl₃ solution (pH = 2.5) in a bottle. In addition, a pH meter probe (from VWR sympHony pH Meters) was inserted via the hole on the bottle cap to achieve a sealed environment. pH values were measured at 1 min intervals for 20 min.

Short-Circuited Current Measurement. Metal nanowire-loaded alumina membrane was sandwiched by two pieces of silicone rubber (upper piece with a fixed area hole to expose the template) and mounted at the bottom of a glass tube with an O-ring seal. Then the TiCl₃ solution was filled into the glass tube with ITO-coated glass inserted. The whole device was under nitrogen protection. Short-circuited currents between the alumina membrane and ITO glass were measured by potentiostat SP-150 from Biologic by applying 0 V between the two electrodes.

Electron Microscopy. SEM images were obtained using the Leo 1530 field emission scanning electron microscope at 3 kV. TEM images (EDS analysis) were collected by a JEOL 2010F Field Emission TEM/STEM with EELS and EDS at 200 kV.

Photodegradation. The photocatalytic activities of the core–shell Ni–TiO₂ nanoparticles were evaluated by degradation of methylene blue (MB) in an aqueous solution under irradiation of ultraviolet (UV) light. Photocatalytic activity experiments were performed at ambient temperature and pressure. A compact (4 W, λ = 365 ± 15 nm) UV lamp (UVP, UVGL-25) was used as the UV light source. Typically, the aqueous MB–catalyst suspension was prepared as follows: in a quartz spectrophotometer cell (VWR 414004-078), 2 mg of sample of the core–shell Ni–TiO₂ catalyst (effective TiO₂ weight about 1 mg based on the shell thickness) was dispersed in 3 mL of MB solution (5 mg/L) by ultrasonication for 1 min. The mixture was stirred for 1 h in the dark to blend well and allow adsorption–desorption equilibrium

before irradiation. The suspension was magnetically stirred before and during illumination. The distance of the quartz cell and the UV light source is maintained at 10 cm. At a certain time interval during the experiment a strong magnet was applied to the bottom of the quartz cell to separate the catalyst; then the solution was analyzed on the basis of MB characteristic optical absorption using a Thermo Scientific GENESYS 10S UV–vis (200–800 nm) to measure the change of MB concentration with irradiation time based on Lambert–Beer's law. The percentage of degradation was indicated as C/C_0 . Here, C is the absorption of MB solution at each irradiation time interval of the main peak of the adsorption spectrum, and C_0 is the absorption of the initial concentration when the adsorption/desorption equilibrium was achieved. For comparison, the photocatalytic activity of the commercial bare TiO₂ nanoparticles (25 nm) was also conducted under the identical experimental conditions.

Electrochemical Test. Electrochemical studies of the Au–TiO₂ core–shell nanowire array were performed in the standard three-electrode system; Ag/AgCl was used as the reference electrode, and Pt foil was used as the counter electrode. Galvanostatic charge/discharge for the lithium-ion insertion study was done by cycling the potential from -0.2 to -2.2 V (from 3 to 1 V vs Li/Li⁺) at a current density of 0.25–1 mA/cm² (corresponds to about 5–20 C charge/discharge rate for Au–TiO₂ core–shell nanowire array) using 1 M LiPF₆ in EC:DEC solution (weight ratio 1:1). The lithium-ion insertion coefficient, x , determines the charge storage capacity of TiO₂, and the maximum value of x is 1, which corresponds to a Ti oxidative state change from +4 to +3. Thus, the calculated theoretical lithium-ion charge capacity of TiO₂ was 335 mAh/g.

BET Measurement. The BET measurements were done by PSL (Pore Science Laboratories) from the Y-Carbon, Inc. Nitrogen was chosen as the adsorptive gas. The analysis bath temperature was held at -195.8 °C.

■ ASSOCIATED CONTENT

📄 Supporting Information

SEM images of Ag nanowires before and after exposure to TiCl₃ solution, dark-field TEM image of TiO₂ nanotube embedded with Pt nanoparticles, estimation/calculation of charge/discharge capacity TiO₂ shell as electrode material, cyclic voltammogram, Ragone plot and cycling performance test of TiO₂ electrode material, effect of TiO₂ thickness on the charge/discharge capacity, photocatalytic performance of Ni–TiO₂ core–shell nanoparticles and commercial TiO₂ nanoparticles, and BET measurements of surface area and pore-size distribution. This material is available free of charge via the Internet at <http://pubs.acs.org>.

■ AUTHOR INFORMATION

Corresponding Author

E-mail: asen@psu.edu

Notes

The authors declare no competing financial interest.

■ ACKNOWLEDGMENTS

We thank Joe Kulik for TEM imaging and analysis. We gratefully acknowledge funding by the U.S. Army (W911NF-06-1-0280) and Air Force Office of Scientific Research (FA9550-10-1-0509).

■ REFERENCES

- (1) Chen, X.; Mao, S. S. *Chem. Rev.* **2007**, *107*, 2891.
- (2) Oregan, B.; Gratzel, M. *Nature* **1991**, *353*, 737.
- (3) Hagfeldt, A.; Gratzel, M. *Chem. Rev.* **1995**, *95*, 49.
- (4) Mor, G. K.; Shankar, K.; Paulose, M.; Varghese, O. K.; Grimes, C. A. *Nano Lett.* **2006**, *6*, 215.
- (5) Osterloh, F. E. *Chem. Mater.* **2008**, *20*, 35.

- (6) Khan, S. U. M.; Al-Shahry, M.; Ingler, W. B. *Science* **2002**, *297*, 2243.
- (7) Mor, G. K.; Shankar, K.; Paulose, M.; Varghese, O. K.; Grimes, C. A. *Nano Lett.* **2005**, *5*, 191.
- (8) Gaya, U. I.; Abdullah, A. H. *J. Photochem. Photobiol. C: Photochem. Rev.* **2008**, *9*, 1.
- (9) Li, F. B.; Li, X. Z. *Chemosphere* **2002**, *48*, 1103.
- (10) Chen, X. B.; Liu, L.; Yu, P. Y.; Mao, S. S. *Science* **2011**, *331*, 746.
- (11) Hagfeldt, A.; Vlachopoulos, N.; Gratzel, M. *J. Electrochem. Soc.* **1994**, *141*, L82.
- (12) Cinnsealach, R.; Boschloo, G.; Rao, S. N.; Fitzmaurice, D. *Sol. Energy Mater. Sol. Cells* **1999**, *57*, 107.
- (13) Lakshmi, B. B.; Dorhout, P. K.; Martin, C. R. *Chem. Mater.* **1997**, *9*, 857.
- (14) Wang, C. C.; Ying, J. Y. *Chem. Mater.* **1999**, *11*, 3113.
- (15) Kasuga, T.; Hiramatsu, M.; Hoson, A.; Sekino, T.; Niihara, K. *Langmuir* **1998**, *14*, 3160.
- (16) Jun, Y. W.; Casula, M. F.; Sim, J. H.; Kim, S. Y.; Cheon, J.; Alivisatos, A. P. *J. Am. Chem. Soc.* **2003**, *125*, 15981.
- (17) Stathatos, E.; Lianos, P.; DelMonte, F.; Levy, D.; Tsiourvas, D. *Langmuir* **1997**, *13*, 4295.
- (18) Yang, P.; Zhao, D.; Margolese, D. I.; Chmelka, B. F.; Stucky, G. D. *Chem. Mater.* **1999**, *11*, 2813.
- (19) Armstrong, A. R.; Armstrong, G.; Canales, J.; Bruce, P. G. *Angew. Chem., Int. Ed.* **2004**, *43*, 2286.
- (20) Sun, X. M.; Li, Y. D. *Chem.—Eur. J.* **2003**, *9*, 2229.
- (21) Bavykin, D. V.; Parmon, V. N.; Lapkin, A. A.; Walsh, F. C. *J. Mater. Chem.* **2004**, *14*, 3370.
- (22) Kavan, L.; Oregan, B.; Kay, A.; Gratzel, M. *J. Electroanal. Chem.* **1993**, *346*, 291.
- (23) Natarajan, C.; Nogami, G. *J. Electrochem. Soc.* **1996**, *143*, 1547.
- (24) Hoyer, P. *Langmuir* **1996**, *12*, 1411.
- (25) Miao, Z.; Xu, D. S.; Ouyang, J. H.; Guo, G. L.; Zhao, X. S.; Tang, Y. Q. *Nano Lett.* **2002**, *2*, 717.
- (26) Mor, G. K.; Varghese, O. K.; Paulose, M.; Grimes, C. A. *Adv. Funct. Mater.* **2005**, *15*, 1291.
- (27) Gong, D.; Grimes, C. A.; Varghese, O. K.; Hu, W. C.; Singh, R. S.; Chen, Z.; Dickey, E. C. *J. Mater. Res.* **2001**, *16*, 3331.
- (28) Roy, P.; Berger, S.; Schmuki, P. *Angew. Chem., Int. Ed.* **2011**, *50*, 2904.
- (29) Tan, L. K.; Chong, M. A. S.; Gao, H. *J. Phys. Chem. C* **2008**, *112*, 69.
- (30) Shi, J. A.; Sun, C. L.; Starr, M. B.; Wang, X. D. *Nano Lett.* **2011**, *11*, 624.
- (31) Liu, R.; Lee, S. B. *J. Am. Chem. Soc.* **2008**, *130*, 2942.
- (32) Liu, R.; Duay, J.; Lee, S. B. *Chem. Commun.* **2011**, *47*, 1384.
- (33) Wang, C.; Yin, L.; Zhang, L.; Liu, N.; Lun, N.; Qi, Y. *ACS Appl. Mater. Interfaces* **2010**, *2*, 3373.
- (34) Zhang, N.; Liu, S. Q.; Fu, X. Z.; Xu, Y. J. *J. Phys. Chem. C* **2011**, *115*, 9136.
- (35) Ding, Y. D. Y.; Wang, Y.; Zhang, L. C.; Zhang, H.; Li, C. M.; Lei, Y. *Nanoscale* **2011**, *3*, 1149.
- (36) Chen, M. S.; Goodman, D. W. *Science* **2004**, *306*, 252.
- (37) Li, H. X.; Bian, Z. F.; Zhu, J.; Huo, Y. N.; Li, H.; Lu, Y. F. *J. Am. Chem. Soc.* **2007**, *129*, 4538.
- (38) Qamar, M.; Kim, S. J.; Ganguli, A. K. *Nanotechnology* **2009**, *20*, 455703.
- (39) Hosseini, M. G.; Momeni, M. M.; Faraji, M. *Electroanalysis* **2010**, *22*, 2620.
- (40) Hirakawa, T.; Kamat, P. V. *J. Am. Chem. Soc.* **2005**, *127*, 3928.
- (41) Liang, Y.-C.; Wang, C.-C.; Kei, C.-C.; Hsueh, Y.-C.; Cho, W.-H.; Perng, T.-P. *J. Phys. Chem. C* **2011**, *115*, 9498.
- (42) Du, J. M.; Zhang, J. L.; Liu, Z. M.; Han, B. X.; Jiang, T.; Huang, Y. *Langmuir* **2006**, *22*, 1307.
- (43) Pastoriza-Santos, I.; Koktysh, D. S.; Mamedov, A. A.; Giersig, M.; Kotov, N. A.; Liz-Marzan, L. M. *Langmuir* **2000**, *16*, 2731.
- (44) Caruso, R. A.; Susha, A.; Caruso, F. *Chem. Mater.* **2001**, *13*, 400.
- (45) Ammar, I. A.; Awad, S. A. *J. Phys. Chem.* **1956**, *60*, 837.
- (46) Hong, Y. Y.; Diaz, M.; Cordova-Figueroa, U. M.; Sen, A. *Adv. Funct. Mater.* **2010**, *20*, 1568.
- (47) Nikoobakht, B.; Wang, Z. L.; El-Sayed, M. A. *J. Phys. Chem. B* **2000**, *104*, 8635.
- (48) Liu, K.; Zhao, N.; Kumacheva, E. *Chem. Soc. Rev.* **2011**, *40*, 656.
- (49) Hibino, M.; Abe, K.; Mochizuki, M.; Miyayama, M. *J. Power Sources* **2004**, *126*, 139.
- (50) Moriguchi, I.; Hidaka, R.; Yamada, H.; Kudo, T.; Murakami, H.; Nakashima, N. *Adv. Mater.* **2006**, *18*, 69.
- (51) Wang, D. H.; Choi, D. W.; Li, J.; Yang, Z. G.; Nie, Z. M.; Kou, R.; Hu, D. H.; Wang, C. M.; Saraf, L. V.; Zhang, J. G.; Aksay, I. A.; Liu, J. *ACS Nano* **2009**, *3*, 907.
- (52) Guo, Y. G.; Hu, Y. S.; Sigle, W.; Maier, J. *Adv. Mater.* **2007**, *19*, 2087.
- (53) Polshettiwar, V.; Luque, R.; Fihri, A.; Zhu, H. B.; Bouhrara, M.; Bassett, J. M. *Chem. Rev.* **2011**, *111*, 3036.
- (54) Agrawal, M.; Gupta, S.; Pich, A.; Zafeiropoulos, N. E.; Rubio-Retama, J.; Jehnichen, D.; Stamm, M. *Langmuir* **2010**, *26*, 17649.